PCCP

View Online
Dynamic Article Links

Cite this: *Phys. Chem. Chem. Phys.*, 2011, **13**, 13295–13304

www.rsc.org/pccp

PAPER

The primary step in the ultrafast photodissociation of the methyl iodide dimer

R. de Nalda,[a] J. Durá,†[bc] J. González-Vázquez,[ab] V. Loriot[ab] and L. Bañares*[b]

Received 10th January 2011, Accepted 1st June 2011
DOI: 10.1039/c1cp20083f

This paper shows the results of combined experimental and theoretical work that have unravelled the mechanism of ultrafast ejection of a methyl group from a cluster, the methyl iodide dimer $(CH_3I)_2$. *Ab initio* calculations have produced optimized geometries for the dimer and energy values and oscillator strengths for the excited states of the A band of $(CH_3I)_2$. These calculations have allowed us to describe the blue shift that had been observed in the past in this band. This blue shift has been experimentally determined with higher precision than in all previously reported experiments, since it has been measured through its effect upon the kinetic energy release of the fragments using femtosecond velocity map imaging. Observations of the reaction branching ratio and of the angular nature of the fragment distribution indicate that two main changes occur in A-band absorption in the dimer with respect to the monomer: a substantial change in the relative absorption to different states of the band, and, more importantly, a more efficient non-adiabatic crossing between two of those states. Additionally, time resolved experiments have been performed on the system, obtaining snapshots of the dissociation process. The apparent retardation of more than 100 fs in the dissociation process of the dimer relative to the monomer has been assigned to a delay in the opening of the optical detection window associated with the resonant multiphoton ionization detection of the methyl fragment.

I. Introduction

Some of the most valued experimental techniques in Chemical Physics developed over the last decade, such as velocity map ion/electron imaging, in particular when coupled with ultrashort laser pulse excitation, provide a powerful tool for the study of photoinitiated processes in the gas phase. Since most of those studies need to be carried out under vacuum, and in conditions of atomic or molecular jets, they have mostly covered the study of single atoms or molecules. Clusters, or aggregates, however, offer a unique chance to study the influence of a weakly bound environment on a photoinitiated process. The "solvent" effect does not necessarily involve subtle changes: even though, typically, inter-molecular distances in van der Waals clusters are large, several examples exist in the literature of a phenomenon known as "concerted" photochemistry,[1,2] *i.e.* reaction routes that are only possible in clusters, since they involve reactions between constituent molecules. While concerted photochemistry is the most extreme case of cluster-specific chemistry, reactions that can take place in the isolated molecule can witness important differences when the molecule is immersed in such an environment. It is this type of study that has been undertaken in the present work, where the ultrafast ejection of a CH_3 group from a UV-irradiated methyl iodide dimer $(CH_3I)_2$ in the so-called A-band has been analyzed and the changes with respect to the analogous process in the isolated molecule have been identified.

Several issues of relevance arise when the time-resolved study of clusters is undertaken. Firstly, clusters constitute systems of larger dimensions, and weakly bounded, whose relaxation times can exceed by far the typical times for the processes under study. Therefore, a fast process like prompt dissociation may be "blind" to configurational changes that only take place after substantial delay. This will be demonstrated in the present work through the study of the fast ejection of a CH_3 fragment from the $(CH_3I)_2$ dimer; the agreement between experiment and theory is only possible if the theoretical calculation is made under the assumption that the remaining $[I\cdots ICH_3]$ species cannot relax to its equilibrium geometry during the dissociation time. In this situation, the kinetic energy acquired by the fast CH_3 fragment does not reflect the expected value at the final surface minimum, but at a position that is closer to the initial surface. Secondly, for excitation into a complex manifold of states, such as is the

[a] *Instituto de Química Física Rocasolano, CSIC, C/Serrano 119, 28006 Madrid, Spain*
[b] *Departamento de Química Física I, Facultad de Ciencias Químicas, Universidad Complutense de Madrid, 28040 Madrid, Spain. E-mail: banares@quim.ucm.es*
[c] *Instituto de Estructura de la Materia, CSIC, C/Serrano 123, 28006 Madrid, Spain*
† Present address: ICFO - Institute of Photonic Sciences, 08860 Castelldefels, Barcelona, Spain.

case in the A-band of CH_3I, solvent-induced energy shifts can change substantially the absorption ratio between states, and this can cause dramatic differences in the final channels. Thirdly, nonadiabatic crossings, delicately dependent on the interaction between electronic and nuclear degrees of freedom, can experience important changes that may, equally, yield strong differences in the output reaction channels. Finally, when product detection is done through resonant multiphoton ionization (REMPI) schemes and a clocking measurement is attempted, it is essential to realize that intermediate states of the REMPI process, which are often Rydberg states of spatially extended nature, can be notably distorted in a cluster medium, even for elongated distances, and this can produce apparent delays in clocking times of the process.

A-band dissociation in CH_3I upon UV light absorption, which causes rupture of the C–I bond, has been a prototype reaction both for theory and experiment, because it unites the simplicity of an almost unidimensional (diatomic-type) bond breakage with the complexity of an ensemble of absorbing states, the presence of nonadiabatic couplings and nontrivial partitions of the available energy among electronic, vibrational and rotational degrees of freedom (see for instance ref. 3–13 and references therein). Photodissociation of CH_3I in the UV (between 220 and 350 nm) proceeds *via* three optically allowed transitions: two weak perpendicular transitions to the $^3Q_1$ and $^1Q_1$ states that correlate with ground-state $I(^2P_{3/2})$, and a strong parallel transition to the $^3Q_0$ state that correlates with spin–orbit excited $I^*(^2P_{1/2})$. In the central part of the absorption band, most of the absorption can be attributed to the $^3Q_0$ state, and the $I(^2P_{3/2})$ fragment observed in the experiments is the result of a non-adiabatic transition at the conical intersection between the $^3Q_0$ and $^1Q_1$ states. Time resolved studies, together with wave packet calculations, have been performed by some of the authors of this work,[11] and have established reaction times for the main channels of this reaction.

Iodine-containing clusters of the type $(RI)_n$ have been the subject of extensive study, mainly because they are an excellent example of concerted photochemistry. In particular, the appearance of I_2 or I_2^+ species after the UV photodissociation of $(CH_3I)_n$ has been studied with a variety of techniques such as time-of-flight[14] or kinetic-energy time-of-flight[15,16] mass spectrometry, velocity-map imaging,[2,17] resonance Raman scattering,[18] laser-induced fluorescence[19–21] or cavity-ring-down spectroscopy.[22,23] The study of the effect of solvation on A-band dissociation of one of the C–I bonds has been explored to a lesser extent, and the main contribution was reported by Donaldson *et al.*,[24] who measured absorption spectra of $(CH_3I)_n$ that showed clear changes with respect to CH_3I monomer spectra. The data were interpreted in light of a model that involved a solvent-induced shift in the potential surfaces relevant for the dissociation dynamics. Later, Tanaka *et al.*[25] made a related observation using low-resolution ion imaging: a lower kinetic energy release in the CH_3 fragments resulting from cluster than from monomer dissociation.

This work presents the first study where the velocity map imaging technique has been employed to study a fast photo-initiated process in a cluster through the use of a femtosecond laser pump–probe scheme. This has permitted us to obtain a chronogram of the fragmentation process, with detailed pictures of the energy distributions, the orientational features and the appearance times of the relevant channels. As will be shown, the work demonstrates that cluster-specific behavior produces crucial changes even in a prompt bond fission. *Ab initio* quantum chemical calculations have been undertaken and provide support for the experimental findings.

II. Methods

Experimental setup

The experimental setup has been described in detail elsewhere[11] and a short description will be provided here. The laser is a chirped-pulse amplification (CPA) Ti:sapphire system delivering 80 fs, 1 mJ pulses centered at 802 nm at 1 kHz repetition rate. The fundamental output is split into two arms in a 80 : 20 splitter. The weaker beam is frequency tripled in a third-harmonic generation unit and provides the 267 nm pump beam for the experiment. The remaining beam is used to pump an optical parametric amplifier (OPA), where signal and idler pulses are generated in a BBO crystal. The signal pulse is later frequency quadrupled to constitute the probe beam around 333.5 nm to detect CH_3 radicals by 2 + 1 REMPI. The bandwidth of both pump and probe lasers is 3 nm FWHM. A PC-controlled, motorized delay stage in the pump arm provides controllable delay between the two pulses. Typical beam energies in the experiment are around 1 μJ per pulse and 3 μJ per pulse for the pump and probe beams, respectively. The time duration of the pump and probe pulses is estimated to be around 120 fs, limited by the observed cross-correlation of around 200 fs. Independent polarization control in each arm is provided by the use of half-wave plates, and telescopes are used to control their focussing geometry on target. The pump and probe laser beams are propagated into the vacuum chamber collinearly and focused with a 25 cm focal length lens into the interaction region of the chamber. Their polarization is kept parallel to the detector face to provide the cylindrical symmetry required for the procedure of Abel inversion of ion images.

The vacuum chamber is divided into three parts: source, ionization and detection. The molecular beam is generated in the source chamber, which is differentially pumped from the other two. During the experiments, CH_3I is kept in a salt/ice bath. A supersonic molecular pulsed beam of CH_3I seeded in Ar (3.5 bar) is formed in a 1 kHz piezoelectric homemade nozzle valve (0.5 mm diameter orifice).[26] By selecting the initial part of the gas pulse or the colder, cluster-rich central part, we can distinguish between the contributions from the monomer alone and those of aggregates. The molecular beam passes through a 0.5 mm skimmer that separates the source chamber from the ionization chamber. Once in the ionization chamber, the molecular beam flies between the repeller and the extractor plates of a gridless ion lens electrode system located perpendicularly to it and to the propagation of the laser beams. The ions created in the interaction region are extracted towards the 60 cm time-of-flight tube at the end of which sits the detector, a dual microchannel plate (MCP) coupled to a phosphor screen. Appropriate voltages to the electrodes are applied so that a velocity mapping configuration[27] is achieved. Optimum velocity

mapping conditions were obtained with $V_{extractor}/V_{repeller}$ = 0.79 ($V_{repeller}$ = 5200 V). By applying a gated voltage to the front plate of the MCP, a selective detection of ion masses can be achieved. The 2D mass-selected images on the phosphor screen are recorded with a Peltier-cooled 12-bit CCD camera and stored in a PC. The velocity, and thus the kinetic energy, of the ions was calibrated using the well-known CH_3 images produced in the photodissociation of CH_3I. In these conditions, the kinetic energy resolution of the apparatus is better than 100 meV at 1 eV kinetic energy release.

The methodology in a typical experiment is as follows: the sample, containing both CH_3I molecules and clusters, is excited into the dissociative A-band by the 267 nm pump beam. After a varying delay, the resulting neutral CH_3 fragment is ionized in a 2 + 1 REMPI process by the probe beam. The ions resulting from the process are mass selected and imaged onto the detector, typically using for the camera an exposure time of 10–60 s, *i.e.* corresponding to the accumulation of some tens of thousands of laser shots. The acquisition and storage process, together with the control of the position of the delay line, is fully PC automatized. The raw images are Abel inverted with the pBasex method[28] where polar coordinates are applied for the inversion.

A typical experimental run produces around 100 Abel-inverted ion images as a function of time. The analysis of this type of data is carried out through the use of a multidimensional fit algorithm that has been described elsewhere.[29] Briefly, it consists of an application of the well-known Levenberg–Marquardt nonlinear regression method to *n*-dimensional data. In the case of the present experiment, except when indicated, angular integration was performed for each of the images, and a 2D (radius, time) fit procedure was applied. For the anisotropy study, a subset of images was temporally integrated, and the resulting image was analyzed in 2D (radius, angle). The use of a multidimensional fit algorithm allows a powerful analysis of images, enabling the distinction of separate contributions to the images through their distinct behavior across the different dimensions.

Ab initio calculations

The combination of CASSCF[30] and MS-CASPT2[31] methods was employed to calculate the ground and excited electronic states (including spin–orbit) of the $(CH_3I)_2$ dimer. This combination was already demonstrated to be a good approximation for the description of CH_3I.[32] In that work, Ajitha *et al.* used a CAS with six active electrons in 4 orbitals including the lone pairs in I and the bonding and antibonding C–I ones with the ANO-RCC basis set.[33–35] In order to reduce the computational cost, the contraction was reduced to a triple-ζ polarization with 4s3p2d1f for C, 3s2p1d for H and 7s6p4d2f1g for I. This contraction with a CAS(6,4) was tested in the CH_3I monomer and applied to describe the dimer with a CAS(12,8). This active space for one of the main conformers of the dimer is shown in Fig. 1. In addition to the CAS(6,4) for the monomer, the same orbitals in the other molecule were added. State Average CASSCF calculations were performed for the singlet and triplet states (3 singlet states and 3 triplet states in the case of the monomer and 9 singlet and 9 triplet states for the dimer)

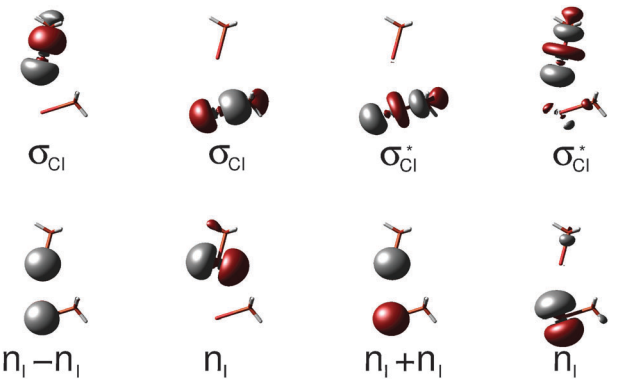

Fig. 1 Active space in the CAS(12,8) calculations. We have included the bonding and antibonding C–I orbitals and the lone pairs in iodine.

and the energies were corrected using MS-CASPT2. In order to avoid intruder states in the MS-CASPT2 calculations, a level shift of 0.2 au was used.[36] Finally, the spin–orbit coupling was taken into account by the AMFI approximation[37] obtaining 12 electronic states for the monomer and 36 for the dimer. The MOLCAS 7.2 code[38] was employed for the CASSCF and CASPT2 calculations.

Considering that geometry optimization is not computationally feasible at the MS-CASPT2 level of theory and that the CASSCF method does not account well for dispersion interaction in van der Waals complexes, the geometries for the ground state stationary points of the monomer and the dimer were optimized at the MP2 level of theory with the aug-cc-pVTZ basis set, similarly to Bogdanchikov *et al.*[39] In the present calculations, the MOLPRO package was used with the same basis set as in ref. 39, but with the pseudopotential for the I atom described in ref. 40. The ground state energies were then calculated for the optimized MP2 geometries using MS-CASPT2. Considering that the CAS method is not size consistent, the basis set superposition error (BSSE) has to be considered in the estimation of the stabilization energy of the dimer. A reference calculation with the two monomers separated by 20 Å was computed using the MP2 geometry of the monomer. However, the BSSE depends on the intermolecular distance and, thus, the problem is not solved by doing such reference calculation. In any case, the BSSE evaluated by Bogdanchikov *et al.*[39] for the ground state of the dimer is about 20% of the global energy of the dimer. If a similar percentage is assumed in the present case, given the similarities of the basis set employed, the qualitative picture derived from the present calculations does not change. To avoid symmetry problems, the geometries were not restricted to a symmetry group, *i.e.* they were optimized in C_1 symmetry.

III. Results and discussion

Conventional time-of-flight-mass-spectrometry (TOF-MS) experiments were carried out in order to characterize relative cluster/monomer densities in the expansion conditions, which favors the formation of clusters (*i.e.* middle part of the gas pulse). Mass spectra were acquired with 70 fs, 800 nm, 10^{12} W cm^{-2} laser pulses, at intensities low enough so that dissociative ionization processes play a lesser role. The result obtained in

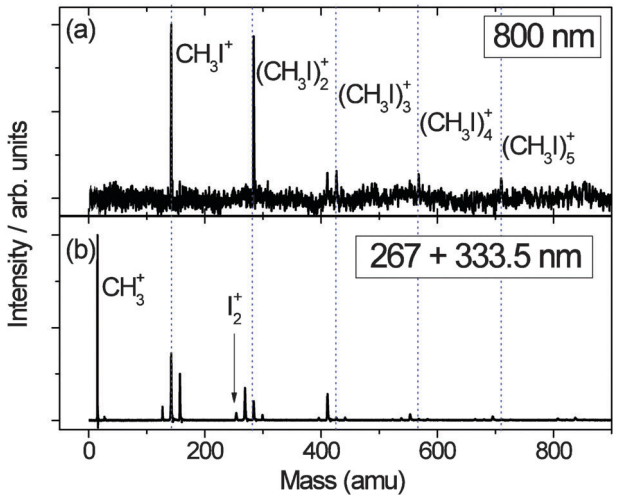

Fig. 2 Mass spectra of CH_3I in clustering conditions, acquired with (a) IR (800 nm) 70 fs laser pulses at relatively low intensity (10^{12} W cm^{-2}). The monomer CH_3I and the dimer $(CH_3I)_2$ are the predominant species, and (b) pump (267 nm) and probe (333.5 nm) laser pulses, separated in time by 4 ps. Fragments resulting from fragmentation appear and the CH_3 peak suffers an intense enhancement due to the 2+1 REMPI process at 333.5 nm.

these expansion conditions is shown in Fig. 2a, where it is clear that the main species are CH_3I and $(CH_3I)_2$, with number densities of the same order of magnitude (the dimer and monomer possess similar ionization potentials,[39,41] although absorption cross sections would be expected to be somewhat higher for the dimer).[14] Larger aggregation is visible, up to $(CH_3I)_5$, but constitutes a low fraction of the detected species. In monomer expansion conditions (*i.e.* initial part of the gas pulse), only the CH_3I monomer is observed in the mass spectrum. Fig. 2b shows the result of an analogous experiment as that shown in Fig. 2a but in a pump–probe configuration with two femtosecond laser pulses (a 267 nm pump and a 333.5 nm probe delayed by 4 ps). The better signal-to-noise ratio in this case allows us to detect more massive clustered species, with aggregation as large as $(CH_3I)_9$, but additional masses resulting from fragmentation are also observed. A clear enhancement in all signal levels is observed with respect to the sum of signals produced by each of the lasers separately. A particularly large enhancement is found for the CH_3^+ peak, which we attribute to resonantly enhanced multiphoton ionization (REMPI) through the 2+1 process *via* the Q branch of the $3p_z(^2A''_2 \leftarrow {}^2A''_2)$ 0_0^0 transition at 333.5 nm. The enhancement observed for all other species is likely to be caused by nonresonant ionization. Apart from the exceptional enhancement of the CH_3^+ signal, the mass spectrum is not dissimilar from that found in ref. 14 with picosecond or ref. 42 with femtosecond excitation, but shows a shift towards the lower-order clusters, probably due to differing expansion conditions. An important observation is the presence of I_2^+ in the mass spectrum, a species that marks the existence of intracluster reactions. In fact, in some cases with nanosecond laser excitation, I_2^+ has been the sole signature of the presence of clusters.[2] In conclusion, the results shown in Fig. 2 indicate that the main component of the cluster distribution is the $(CH_3I)_2$ dimer. In the rest of this paper, we will assume that the distinct sharp features observed in the ion images, apart from those directly attributed to the photodissociation of the monomer, are due to the $(CH_3I)_2$ species. Participation to the signal from larger clusters present in the expansion is also evident in the images in the form of broad featureless contributions.

Results corresponding to resonant detection of the CH_3 fragment that appears upon dissociation will now be presented. In A-band dissociation of the CH_3I monomer, the CH_3 fragment can appear in correlation with the iodine atom either in its ground state $I(^2P_{3/2})$, or its spin–orbit excited state $I^*(^2P_{1/2})$. Because of the large spin–orbit splitting in iodine (0.943 eV), these channels appear as two distinct components in the kinetic energy release (see for instance ref. 8, 9, 11 and 43). Fig. 3a shows the Abel-inverted image corresponding to CH_3 in conditions where no contribution from clusters is detected (*i.e.* the early part of the gas pulse), and for a long delay time between the pump and probe lasers, *i.e.* once dissociation is complete. Mainly vibrationless ($\nu = 0$) CH_3 is detected in this case due to two-photon resonant enhancement of the 0_0^0 band of the $3p_z(^2A''_2 \leftarrow {}^2A''_2)$ transition at 333.5 nm. The two components mentioned above appear as the two main rings in the image, or as the two main peaks in the kinetic energy distribution shown in Fig. 3c. There is a much weaker intermediate ring that corresponds to CH_3 in its $\nu_1 = 1$ state (ν_1 being the symmetric stretch mode) in correlation with $I(^2P_{3/2})$, which can be observed because of the spectral proximity of the 1_1^1 band to the 0_0^0 band and the broadband nature of the femtosecond laser probe pulse. The nonstructured contribution in the center of the image, *i.e.* low kinetic energy, is attributed to a combination of multiphoton ionization processes induced by the pump and probe pulses. These results have been previously presented by our group in ref. 11 and 43. The colored lines in Fig. 3c show the different contributions employed to fit the experimental

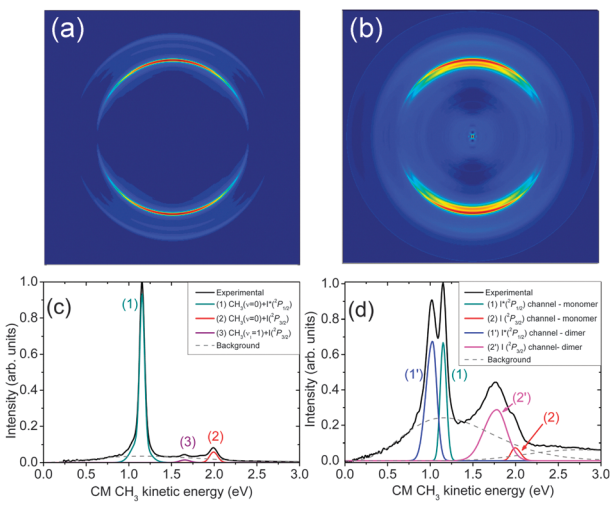

Fig. 3 (a) and (b) Abel inverted experimental CH_3^+ images obtained upon excitation of (a) CH_3I, and (b) a mixture of CH_3I and $(CH_3I)_2$, by two laser pulses: pump pulse at 267 nm and probe pulse, delayed by 1.5 ps, at 333.5 nm, for CH_3 (2+1) REMPI. (c) and (d) Corresponding center-of-mass kinetic energy distributions of CH_3. Experimental data are shown together with simulated curves for the several contributions observed. The separate pump and probe laser contributions have been subtracted from the total signal in both the images and kinetic energy distributions.

distribution. The sum of all the contributions reveals an almost perfect agreement with the experimental curve.

In conditions where cluster presence is important, the corresponding CH_3 image, also taken for a long delay time between the pump and probe laser pulses, appears as is shown in Fig. 3b, with a center-of-mass kinetic energy distribution shown in Fig. 3d. Contributions in the kinetic energy distribution related to A-band dissociation of both the monomer and the dimer appear on the same image, due to the simultaneous presence of both species. Comparison of Fig. 3a and b indicates that the presence of clusters introduces three new contributions to the image. One is a broad, structureless component that can be seen approximately from 0 to $\sim$3 eV and that can be fitted as the sum of two Gaussian distributions on the velocity axis, peaking at $\sim$1.2 eV and $\sim$3 eV. The other two are two new rings (peaks 3 and 4 in Fig. 3d), which appear with a lower kinetic energy release compared with those of the monomer (peaks 1 and 2 in Fig. 3c), broadened in energy and with a larger ratio between the high-KER (KER: kinetic energy release) component ($I(^2P_{3/2})$ channel in the monomer) and the low-KER component ($I^*(^2P_{1/2})$ channel in the monomer). For the low-KER channel, the contributions from the monomer and dimer are clearly distinguishable, but this is no longer the case for the high-KER channel, which appears very significantly broadened and more intense, so much that the monomer $I(^2P_{3/2})$ channel only appears as a shoulder in the high-KER area of the dimer peak. The weaker $CH_3(\nu_1 = 1)$ + $I(^2P_{3/2})$ channel can no longer be observed in these conditions.

Both the experimental observations and the theoretical calculations that will be described below point to the idea that the two new rings observed in the CH_3^+ images correspond to A-band dissociation of the $(CH_3I)_2$ dimer, where the CH_3 fragment is formed in correlation with either the $[I\cdots CH_3I]$ species (high-KER contribution) or the $[I^*\cdots CH_3I]$ species (low-KER contribution). In this scenario, we will refer to the "$I(^2P_{3/2})$ channel" and the "$I^*(^2P_{1/2})$ channel" when describing dimer dissociation.

A-band dissociation in the dimer can appear modified for several reasons, the stabilization energy in the dimer and the different degree of rotational excitation in the outgoing fragments being the most obvious causes of change. The reduction in the kinetic energy of the CH_3 fragment in correlation with $I^*(^2P_{1/2})$ observed in this work is 0.12 $\pm$ 0.01 eV, which would correspond, in the absence of other effects, to a decrease in the total available energy of 0.13 eV (or approximately 1050 cm^{-1}). In the $I(^2P_{3/2})$ channel, we observe a shift of 0.20 $\pm$ 0.04 eV, with a larger uncertainty due to the larger width of this peak. As to the effect of rotation, it is clear from the larger energy width of the peaks associated with dimer dissociation that a significantly larger degree of rotational excitation is present, while no distinction can be made as to whether it corresponds to the light outgoing CH_3 fragment or to the $[I/I^*\cdots ICH_3]$ co-fragment, as both imply a reduction of the total available kinetic energy. Actually, vibrational excitation in the ν_1 mode of the CH_3 fragment cannot be ruled out.

In addition, a significant difference in the anisotropy observed for the monomer and dimer must be noted. A-band absorption is a one-photon process, where the angular dependence of the intensity is given by $I(\theta) = \sigma/4\pi[1 + \beta P_2(\cos\theta)]$,[44] where σ is the total absorption cross section, θ is the angle between the polarization axis of the photolysis laser and the fragment velocity vector, β is the anisotropy parameter, and $P_2(\cos\theta)$ is the second Legendre polynomial. Through the use of the multidimensional fit procedure described in Section II, it has been possible to discriminate the angular character of the different contributions. Asymptotic β values obtained in this manner for the monomer contributions (2.0 $\pm$ 0.2 for the $I^*(^2P_{1/2})$ channel and 1.8 $\pm$ 0.2 for the $I(^2P_{3/2})$ channel) are consistent with the literature,[4,11] and correspond to a purely parallel transition. The $I^*(^2P_{1/2})$ channel of the dimer does not show differences, with a β value of 2.0 $\pm$ 0.2, which indicates that no loss of orientational preference happens upon dimerization. However, the $I(^2P_{3/2})$ channel in the dimer does show a pronounced decrease in the observed anisotropy, with a β value of 1.0 $\pm$ 0.3. The implications of this observation will be discussed below.

One more feature marks a difference between monomer and dimer dissociation results in the asymptotic situation: the dramatic increase in the $I(^2P_{3/2})/I^*(^2P_{1/2})$ ratio observed through the $CH_3(\nu = 0)$ fragment, from values of 0.14 $\pm$ 0.05 for the monomer to 0.72 $\pm$ 0.05 for the dimer. Even though this value for the $I(^2P_{3/2})/I^*(^2P_{1/2})$ ratio in the dimer obtained here is remarkably similar to that reported by Syage,[45,46] this cannot be directly compared, since the values reported by Syage refer to direct measurement of the free I atom after dissociation, whereas here we are measuring the $I(^2P_{3/2})/I^*(^2P_{1/2})$ ratio derived from the kinetic energy distribution in the CH_3 fragment. The companion I atom could—and indeed does—undergo subsequent chemistry within the cluster and flip its spin–orbit state. Analogous measurements were performed by tuning the probe laser to 329.5 and 325.8 nm, which constitute a resonant probe of $CH_3(\nu_2 = 1)$ and $CH_3(\nu_2 = 2)$, respectively (ν_2 being the umbrella mode of CH_3). A dramatic change of the $I(^2P_{3/2})/I^*(^2P_{1/2})$ ratio, in the same direction as that just described for $CH_3(\nu = 0)$, was also observed in both cases.

The decrease of the anisotropy of the $I(^2P_{3/2})$ channel in the dimer and the large change in the branching ratio need to be discussed conjointly. An increase of the $I(^2P_{3/2})/I^*(^2P_{1/2})$ ratio could be related to either a change in the main absorbing states or in the efficiency of the coupling in the nonadiabatic crossing. Since the other possibly participating states, $^1Q_1$ and $^3Q_1$, are of perpendicular nature, in contrast to the parallel $^3Q_0$ state, an examination of the change in anisotropy should permit the distinction between the two phenomena. If we consider that the $I(^2P_{3/2})$ fragment observed is originated partly through absorption to $^3Q_0$ followed by crossing to $^1Q_1$, and partly through direct absorption to one of the perpendicular states ($^3Q_1$ or $^1Q_1$), then the resulting anisotropy is expected to reflect a mixture of parallel ($\beta = 2$) and perpendicular ($\beta = -1$) character. From the observation of an experimental β value of 1.0 $\pm$ 0.3, a ratio of approximately 2 : 1 is extracted for those two routes. This is an important result, since it indicates that the participation of absorption of the perpendicular states is not negligible, as was the case for the monomer at 267 nm excitation; instead, it accounts for approximately 1/3 of the total absorption at this wavelength. However, this alone cannot account for an increase in the $I(^2P_{3/2})/I^*(^2P_{1/2})$ ratio from 0.14 $\pm$ 0.05 for the monomer to 0.72 $\pm$ 0.05 for the dimer.

From the combined values of ratios and anisotropy, we conclude that the efficiency of the nonadiabatic crossing approximately doubles in the dimer with respect to the monomer.

In order to rationalize the differences observed in the photodissociation dynamics between the dimer and the monomer mentioned above, we have performed *ab initio* calculations for ground and excited electronic states of both the monomer and the dimer. In a previous study by Bogdanchikov *et al.*,[39] two $(CH_3I)_2$ conformers corresponding to Head–Head (HH) and Head–Tail (HT) structures were predicted at the MP2 level of theory. Using those structures as a starting point, we have reoptimized the geometry at the same MP2 level of theory with no symmetry restrictions. Fig. 4 shows the present MP2 geometry optimizations. Both HH and HT structures are in good agreement with the geometries found by Bogdanchikov *et al.*[39] However, the I–I and C–C distances are found to be somewhat smaller in the present calculations. The reason for the discrepancies can be due to the different I-atom pseudopotential employed in the present case.

The electronic energies of the two conformers were calculated with perturbation theory MS-CASPT2 using the MP2 geometries. Table 1 shows the calculated MS-CASPT2 electronic energies for the monomer and dimer both at the ground state equilibrium distance and for a large distance between the CH_3 moiety and the rest of the molecule. Through inspection of the energy of the ground electronic state, it is clear that the HT dimer is the most stable conformer. We observe a stronger stabilization than in the MP4(SDTQ)//MP2 calculation of ref. 39: instead of 0.11 eV and 0.10 eV for the HT and HH configurations (not including the zero point energy correction), respectively, we obtain 0.31 eV and 0.26 eV, which are also larger than the experimental determinations.[47] Interestingly, the MS-CASPT2 stabilization energies obtained for both conformers using the geometries reported by Bogdanchikov *et al.*[39] are 0.33 eV and 0.28 eV. Thus, the different values for the stabilization energies

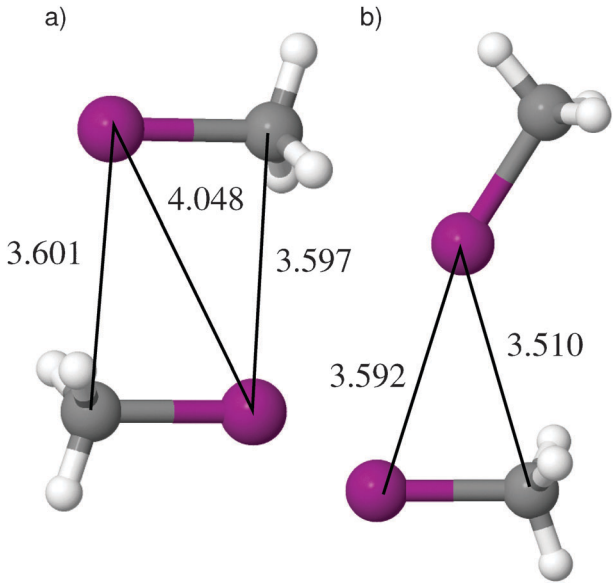

Fig. 4 Optimized geometries for the two conformers of the $(CH_3I)_2$ dimer ground state calculated at MP2 level of theory: (a) Head–Tail and (b) Head–Head conformers.

obtained in the present work in comparison with those reported in ref. 39 are attributed to the different *ab initio* methodology employed for the computation of the ground state energies.

Concerning the excited state energies, we calculated the monomer alone with the same methodology. As in previous works,[10,32,48] the first five states at the equilibrium geometry are assigned to the doubly degenerated states $^3Q_2$ and $^3Q_1$ (4.44 and 4.59 eV), followed by the states $^3Q_{0-}$ (4.95 eV), $^3Q_{0+}$ (5.04 eV) and finally the doubly degenerated state $^1Q_1$ (5.26 eV). Given the oscillator strength values, it is clear that the $^3Q_2$ and $^3Q_{0-}$ are dark states. In the dissociation limit, where the CH_3 group and the I-atom are separated, there are only two states

Table 1 MS-CASPT2 energies (E) of the monomer and dimer (in eV) at the ground state (GS) equilibrium distance and in the dissociation region calculated from the geometries optimized at the MP2 level of theory (see text for details). Both Head–Tail (HT) and Head–Head (HH) conformers of the dimer are presented. In the dissociation limit, the HH conformer yields two different structures depending on the CH_3 fragment which flies apart and we denote the two structures as HH-lin and HH-pyr (see text for details). For the equilibrium geometries, the oscillator strength f (in atomic units) and the state assignment are shown

GS equilibrium distance							Dissociation			
	Monomer		Dimer HT		Dimer HH		Monomer	HT	HH-lin	HH-pyr
	E	f	E	f	E	f	E	E	E	E
GS	0.00		−0.31		−0.26		2.71	2.87	2.87	2.77
$^3Q_2$	4.44	0.000000	4.63	0.0	4.61	0.000003	2.71	2.89	2.89	2.79
			4.63	0.0	4.61	0.000021	2.71	2.89	2.90	2.79
	4.44	0.000000	4.65	0.0	4.73	0.003750	2.74	2.90	2.90	2.79
			4.65	0.000002	4.76	0.002326	2.74	2.96	2.93	3.04
$^3Q_1$	4.59	0.001456	4.75	0.000021	4.77	0.000004	2.74	2.96	2.93	3.05
			4.76	0.000122	4.78	0.000305	2.74	2.98	2.95	3.06
	4.59	0.001456	4.77	0.005373	4.91	0.002401	2.74	2.98	2.95	3.06
			4.79	0.004045	4.91	0.002563	3.58	3.76	3.75	3.77
$^3Q_{0-}$	4.95	0.000133	5.11	0.0	5.10	0.000007	3.58	3.76	3.75	3.77
			5.13	0.000002	5.19	0.000857	3.58	3.77	3.75	3.77
$^3Q_{0+}$	5.04	0.008052	5.21	0.000231	5.26	0.000013	3.60	3.78	3.76	3.79
			5.23	0.000015	5.35	0.012353				
$^1Q_1$	5.25	0.008198	5.33	0.000170	5.35	0.004141				
			5.37	0.025147	5.37	0.016631				
	5.27	0.000000	5.38	0.001994	5.53	0.014022				
			5.39	0.017901	5.53	0.008947				

depending on the spin of the I-atom. The energy difference between these two channels is 0.9 eV, which corresponds to the I-atom splitting due to the spin–orbit coupling, and the dissociation energy is 2.71 eV. The reduction of the basis size to a triple-ζ (important to reduce the computational effort for the dimer) overestimates the excitation and dissociation energies by about 0.1–0.3 eV depending on the value when comparing with Ajitha *et al.*[32] or Alekseyev *et al.*[10] Similar discrepancies are found with respect to experimental values. For instance, the dissociation energy was measured to be 2.41 ± 0.02 eV.[9]

In the dimer, the two molecules can be excited separately and thus the electronic states are duplicated (see Table 1). Due to the vicinity of the companion molecule, the vertical excitations in the dimer are shifted, in general, to higher values. Typically, a shift of around 0.2 eV is observed for both conformers. This is related to the fact that the ground state is more efficiently stabilized than the excited states. Indeed, it had been experimentally shown in the literature that the A-band in $(CH_3I)_2$ suffers a blue-shift. Qualitatively, it had been understood in terms of the ground state dimer being stabilized by a dipole–dipole interaction, while the molecular dipole is weakened by the valence state transition, which involves the promotion of an electron located mainly on the I atom to an antibonding molecular orbital. With a lower dipole–dipole interaction, the dimer in the valence state will not be as stabilized as in the ground electronic state. Donaldson *et al.*[24] reported in 1987 an experimental shift of the peak of the absorption band by around 500–1000 cm^{-1} in conditions of dimer formation with respect to monomer-only conditions. This value is compatible with the value of about 0.2 eV (1600 cm^{-1}) found here.

In order to compare available energies with the experimental data, the dissociation limit must be carefully defined. Both for the monomer and the dimer, the CH_3 fragment can relax during the fast dissociation. However, whereas the co-fragment of CH_3 in the monomer is the I atom, which does not undergo any relaxation process, the co-fragment of CH_3 for the dimer is the $[I\cdots ICH_3]$ species. This species will necessarily undergo geometry relaxation processes after the fast ejection of the CH_3 fragment, but these are expected to happen in time scales larger than CH_3 dissociation, so that the kinetic energy in the CH_3 fragment will not reflect relaxation. Consequently, the dissociation limit in the dimer case is defined allowing the relaxation of the ejected CH_3, but freezing the rest of the molecule. It is using this definition that Table 1 shows the potential energy of the products. Notice that for the HH conformer, two different $[I\cdots ICH_3]$ species with different geometries are obtained depending on what CH_3 fragment is eliminated. The difference between the two structures is the orientation of the remaining I-atom with respect to the other CH_3I molecule. In one case, the structure is almost linear while in the other it is pyramidal, that we will refer to as HH-lin and HH-pyr, respectively. This is not the case for the HT conformer where the two CH_3I molecules are practically parallel.

In the case of the monomer, the lower lying states in the dissociative region are connected with the spin quantum states of $I(^2P_{3/2})$ and $I^*(^2P_{1/2})$, with a difference of about 0.9 eV between them. A significant change, however, can be observed for the relative energy with respect to the equilibrium geometry, which is found to be 2.9 eV for the HT and HH-lin dimers and 2.8 eV for the HH-pyr dimer. These dissociation energies are higher than those found for the monomer (2.7 eV). This will necessarily imply that lower kinetic energies are available for the fragmentation products.

Using a 267 nm laser, the system absorbs 4.64 eV, and is excited mainly to the $^3Q_{0+}$ electronic state. In this fast dissociation process, with low internal excitation of the fragments, the velocity of the fragments is defined by the potential energy in the dissociation limit. In the case of the monomer, we can assign the kinetic energy in the fragments directly as 1.0 and 1.9 eV ($I(^2P_{3/2})$ and $I^*(^2P_{1/2})$ channels). These results are in good agreement with previous experiments and dynamical calculations,[11] as well as the results presented in this paper. However, in the dimer, for which we have to consider the HH and HT conformers, there is a decrease, with expected kinetic energies of 0.9 eV (in both conformers) for the $I^*(^2P_{1/2})$ channel and 1.8 eV (HT and HH-lin) for the $I(^2P_{3/2})$ channel. This energy difference of *ca.* 0.1 eV with respect to the monomer is consistent with the shift in the kinetic energy (0.13 ± 0.1 eV for the $I^*(^2P_{1/2})$ channel, 0.22 ± 0.04 eV for the $I(^2P_{3/2})$ channel) observed in this work for dimer dissociation with respect to monomer dissociation. Fig. 5 shows the energy diagram for the monomer and dimer species, together with the expected available energies upon one-photon absorption at 267 nm.

Finally, it must be noted that under dimerization the electronic energy of the $^3Q_1$ state increases, which moves it closer to resonance with the 267 nm photon. Thus, a larger contribution of this state to the absorption and an increase of the $I(^2P_{3/2})$ channel products with perpendicular character are expected, in agreement with the experimental findings (I/I* ratio and anisotropy) described above.

Further information can be obtained by time-resolved detection. Fig. 6 shows a series of kinetic energy distributions as a function of delay time between the laser pulses. The two most intense peaks, appearing close together and most clearly visible at times later than 400 fs, correspond to the $I^*(^2P_{1/2})$

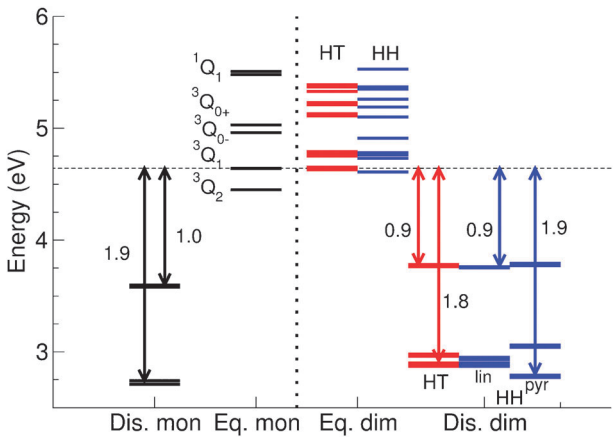

Fig. 5 Energy diagram showing the main states involved in the photodissociation of CH_3I and $(CH_3I)_2$ upon absorption of one UV photon at 267 nm. Both equilibrium and dissociation states are shown. All energy values are plotted relative to the ground state of each species. Total available energies expected for the process are indicated with double arrows.

channel for the dimer (lower kinetic energy) and the monomer (higher kinetic energy). The next component is the broad I channel, where dimer and monomer contributions can only be distinguished for very early times. Interestingly, a weak feature is observed in the kinetic energy distributions in between the contributions from the monomer and the dimer for the I* and I channels, starting at 400 fs delay time and disappearing at 1200 fs, which changes its kinetic energy from larger to smaller values as delay time increases. We believe that this feature is due to Coulomb repulsion within the cluster. However, more experiments are underway in order to clarify the origin of this moving peak in the kinetic energy distribution.

It is clear from Fig. 6 that the contributions due to monomer dissociation appear significantly earlier than those due to dimer dissociation. In order to obtain quantitative measurements of this temporal shift, we have employed a 2D (time, energy) fit to the data in order to extract the separate time behavior of each of the components. Fig. 7 shows the time evolution in the detection of CH_3 coming from the monomer in the $I^*(^2P_{1/2})$ channel, and also from the dimer in both the $I(^2P_{3/2})$ and $I^*(^2P_{1/2})$ channels. A transient shown for a given component is the result of the integrated signal difference between the complete experimental speed distribution and the speed distribution obtained upon adding all the other fitted components.

In a previous experiment,[11] we measured a clocking time for the $CH_3(\nu = 0) + I^*(^2P_{1/2})$ channel in the monomer of 80 ± 20 fs. The time zero of the graph has been established in accordance with this previous value. As is shown in Fig. 7, we obtained a clocking value for the $I(^2P_{3/2})$ channel in the dimer of 218 ± 40 fs, followed by the $I^*(^2P_{1/2})$ channel, with a clocking time of 224 ± 20 fs. Two issues are of importance in reference to dissociation of the dimer: on one hand, the time difference between the two channels ($I(^2P_{3/2})$ and $I^*(^2P_{1/2})$) is compatible with the value that had been obtained previously for the monomer (given the considerable uncertainty in the clocking time of the $I(^2P_{3/2})$ channel in the dimer). On the other hand, however, the absolute values are significantly longer. The fact that the monomer and dimer can be measured simultaneously allows a small error in the determination of this difference, which we estimate in 144 ± 20 fs. Interestingly, the rise time of the dimer transients for both I and I* channels is somewhat faster than that for the I* channel of the monomer. A possible explanation for this difference is related with the effect of dimerization on the steepness of the potential energy surfaces involved in the photodissociation process. A more steep potential energy curve upon dimerization would imply a faster rise time in the dimer transients.

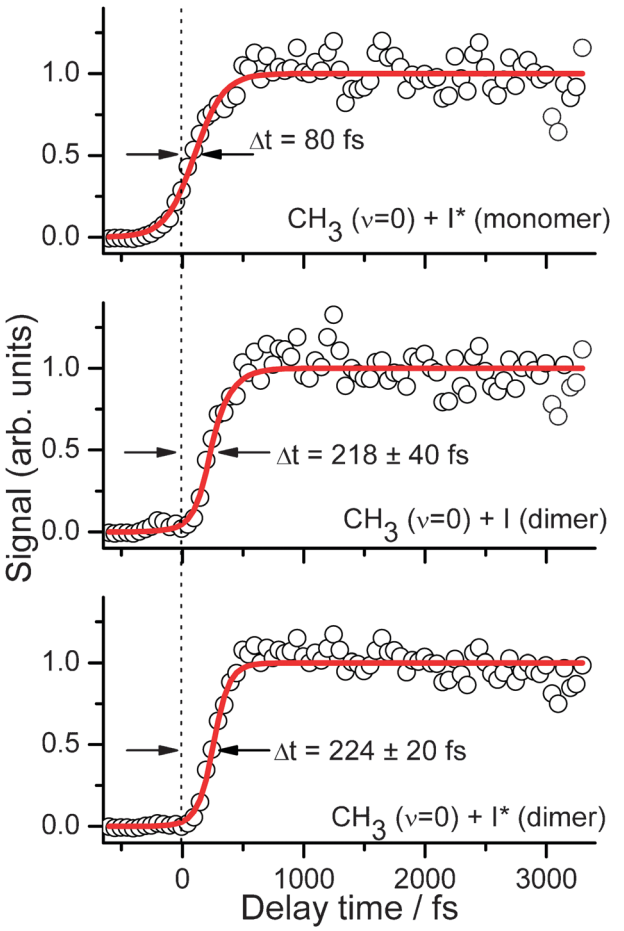

Fig. 7 Transients showing appearance times of the observed channels yielding $CH_3(\nu = 0)$ for both monomer and cluster species. Open circles show the amplitudes of each of the contributions (see text for details); solid lines show the fitted curves.

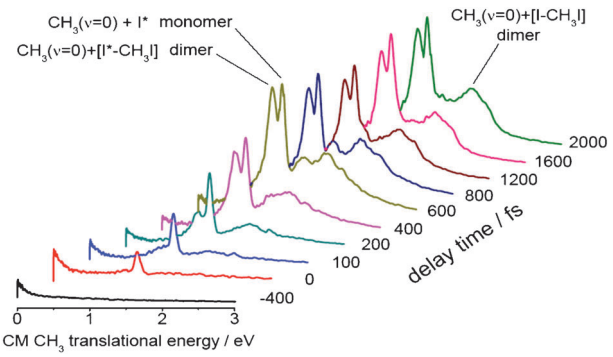

Fig. 6 Series of kinetic energy distributions obtained for pump–probe irradiation of a $CH_3I/(CH_3I)_2$ sample (pump: 267 nm, probe: 333.5 nm) as a function of delay time, obtained through Abel inversion of recorded images. For the lower speed component ($I^*(^2P_{1/2})$ channel), at around 1 eV, monomer and dimer contributions are clearly distinguishable. This is no longer the case for the higher speed component ($I(^2P_{3/2})$ channel), where the width of the peak and the dominance of the dimer contribution obscure the direct observation of the monomer peak, except at short times, where both contributions are visible. It is interesting to note that dimer contributions appear significantly later in time than monomer contributions (see text for discussion).

Similar measurements as a function of time were performed by tuning the probe laser to 329.5 and 325.8 nm, *i.e.* probing the appearance of $CH_3(\nu_2 = 1)$ and $CH_3(\nu_2 = 2)$, respectively. As in the case of $CH_3(\nu = 0)$, a clear delay was observed in the dimer channels with respect to the monomer channels. The magnitude of this delay was comparable to the $CH_3(\nu = 0)$ case, although lower precision was possible due to the poorer signal-to-noise ratios.

The above data provide detailed information about the mechanisms taking place upon A-band dissociation in the $(CH_3I)_2$ dimer. Data obtained from the formation of the free

CH_3 fragment show clearly that a blue shift occurs upon dimerization. The magnitude of the resulting decrease of the available energy in the dissociation process has been satisfactorily reproduced with MS-CASPT2 calculations. In the dimer, the CH_3 radical is able to escape with relatively minor steric impediments. A fast emission of the CH_3 radical upon A-band absorption in the dimer had already been proposed as a first step,[15,16] although, to our knowledge, it had never been observed directly in real time before.

The time delay for free CH_3 observation is still short in the dimer ($\sim$220 fs) but clearly delayed with respect to monomer dissociation ($\sim$80 fs). If the decrease in available energy, due to the blue shift of the band, is taken into account, calculated delays of $\sim$10 fs are obtained classically, indicating that this is clearly insufficient to explain the experimental measurement. On the other hand, this delay could be related to changes in the probing step. In particular, we have considered in detail the influence of the fact that resonant CH_3 probing is done through a 2+1 REMPI process *via* a Rydberg state. This is a state of spatially extended character, and during the first phases of dissociation, it is situated in the vicinity of the $[I\cdots ICH_3]$ moiety, where close-lying Rydberg states can be present. In this situation, the resonance could be significantly perturbed by the nearby presence of $[I\cdots ICH_3]$, so that the CH_3 radical would only appear as "free" after an elongated distance (*i.e.* time).

In order to obtain an estimate of the apparent delay induced by this effect, we have performed a CASSCF calculation aimed at describing the effect of the $[I\cdots ICH_3]$ species in the Rydberg electronic states of the ejected CH_3 group. A reduced model was employed for this purpose, where only two CH_3 groups are considered. The energy of the Rydberg $3p_z$ state is calculated as a function of the distance between the two CH_3 groups. In order to carry out this calculation, we removed all I orbitals (I atoms are not included in the model) so that only the *n* electrons of the two CH_3 groups are included in the active space. We consider configurations where these two electrons can be in the *n* orbitals and in the 3s and 3p Rydberg orbitals, so a CAS(2,10) was employed. As a function of the distance between the two centers-of-mass, we have obtained a potential energy curve that shows significant distorsion for elongated distances. This necessarily implies that the optical window for the REMPI transition employed to detect the appearance of the CH_3 fragment will not be open until the distance is sufficiently long so that this distorsion is negligible (at least, of the order of the bandwidth of the probe laser). A classical 1D dynamic calculation was performed under the simplification that the CH_3 dynamics took place on the $^3Q_{0+}$ monomer surface (shifted by 0.12 eV to account for the blue shift of the band), but the probe laser absorption could only take place once the $3p_z(^2A''_2 \leftarrow {}^2A''_2)$ 0_0^0 transition in CH_3 became resonant under the influence of the nearby presence of the other CH_3. For the estimation of the distances CH_3–CH_3, an axial CH_3–I recoil and a HT geometry for the cluster were assumed. This calculation produced a delay of $\sim$80 fs for the $I^*(^2P_{1/2})$ channel with respect to the situation where distorsion of the Rydberg state of CH_3 does not occur. Even though it is somewhat below the experimental finding of 144 $\pm$ 20 fs, we believe that the fact that it is of the same order indicates that this is the main mechanism producing a delay in the apparent dissociation times for the dimer. We believe that this effect, where a substantial delay occurs in the time opening of the optical detection window, needs to be taken into account whenever resonant probing is employed, especially for large molecules, and in particular clusters, where intermediate orbitals used for the resonant transition can be substantially modified by the nearby presence of a similar moiety.

IV. Conclusions

This work shows that even the influence of a weakly bound environment can have profound influences on a molecular dissociation process. We have chosen a phenomenon (fast ejection of a CH_3 fragment from a $(CH_3I)_2$ dimer) that would not seem prone to showing this effect, due to the extremely fast nature of the dissociation and the weak bond between the two CH_3I molecules. Nevertheless, dramatic changes both in the absorbing states and in the strength of nonadiabatic couplings between them have been detected. For this system, it has been possible to carry out *ab initio* calculations that have produced results compatible with the experimental findings and have helped to rationalize them. It is expected that these cluster-related effects will be even more important in slower processes and more tightly bound systems.

Acknowledgements

This work has been financed by the Spanish MICINN through Grant No. CTQ2008-02578/BQU, and Consolider program "Science and Applications of Ultrafast Ultraintense Lasers" No. CSD2007-00013. We also acknowledge the support from the European Marie Curie Initial Training Network Grant No. CA-ITN-214962-FASTQUAST. JGV acknowledges MICINN for a Juan de la Cierva contract. VL acknowledges CSIC for a JAE-Doc contract and EU for an ER contract. This research has been performed within the Unidad Asociada "Química Física Molecular" between Departamento de Química Física of UCM and CSIC. The facilities provided by the Centro de Asistencia a la Investigación de Espectroscopia Multifotónica y de Femtosegundo (UCM) are gratefully acknowledged.

References

1 D. E. Folmer, E. S. Wisniewski, S. M. Hurley and A. W. Castleman Jr, *Proc. Natl. Acad. Sci. U. S. A.*, 1999, **96**, 12980.
2 K. V. Vidma, A. V. Baklanov, E. B. Khvorostov, V. N. Ishchenko, S. A. Kochubei, A. T. J. B. Eppink, D. A. Chestakov and D. H. Parker, *J. Chem. Phys.*, 2005, **122**, 204301.
3 A. Gedanken and M. D. Rowe, *Chem. Phys. Lett.*, 1975, **34**, 39.
4 R. O. Loo, H. P. Haerri, G. E. Hall and P. L. Houston, *J. Chem. Phys.*, 1989, **90**, 4222.
5 A. D. Hammerich, U. Manthe, R. Kosloff, H. D. Meyer and L. S. Cederbaum, *J. Chem. Phys.*, 1994, **101**, 5623.
6 B. R. Johnson, C. Kittrell, P. B. Kelly and J. L. Kinsey, *J. Phys. Chem.*, 1996, **100**, 7743.
7 Y. Amatatsu, S. Yabushita and K. Morokuma, *J. Chem. Phys.*, 1996, **104**, 9783.
8 A. T. J. B. Eppink and D. H. Parker, *J. Chem. Phys.*, 1998, **109**, 4758.
9 A. T. J. B. Eppink and D. H. Parker, *J. Chem. Phys.*, 1999, **110**, 832.

10 A. B. Alekseyev, H. Liebermann, R. J. Buenker and S. N. Yurchenko, *J. Chem. Phys.*, 2007, **126**, 234102.
11 R. de Nalda, J. Durá, A. García-Vela, J. G. Izquierdo, J. González-Vázquez and L. Bañares, *J. Chem. Phys.*, 2008, **128**, 244309.
12 J. Durá, R. de Nalda, G. A. Amaral and L. Bañares, *J. Chem. Phys.*, 2009, **131**, 134311.
13 L. Rubio-Lago, A. García-Vela, A. Arregui, G. A. Amaral and L. Bañares, *J. Chem. Phys.*, 2009, **131**, 174309.
14 J. A. Syage and J. Steadman, *Chem. Phys. Lett.*, 1990, **166**, 159.
15 D. Zhong, P. Y. Cheng and A. H. Zewail, *J. Chem. Phys.*, 1996, **105**, 7864.
16 D. Zhong and A. H. Zewail, *J. Phys. Chem. A*, 1998, **102**, 4031.
17 K. V. Vidma, A. V. Baklanov, Y. Zhang and D. H. Parker, *J. Chem. Phys.*, 2006, **125**, 133303.
18 P. G. Wang, Y. B. Zhang, C. J. Ruggles and L. D. Zeigler, *J. Chem. Phys.*, 1990, **92**, 2806.
19 Y. B. Fan and D. J. Donaldson, *J. Phys. Chem.*, 1992, **96**, 19.
20 Y. B. Fan and D. J. Donaldson, *J. Chem. Phys.*, 1992, **97**, 189.
21 Y. B. Fan, K. L. Randall and D. J. Donaldson, *J. Chem. Phys.*, 1993, **98**, 4700.
22 F. Ito and T. Nakanaga, *J. Chem. Phys.*, 2003, **119**, 5527.
23 F. Ito, H. Ohmura and T. Nakanaga, *Chem. Phys. Lett.*, 2006, **420**, 157.
24 D. J. Donaldson, V. Vaida and R. Naaman, *J. Chem. Phys.*, 1987, **87**, 2522.
25 Y. Tanaka, M. Kawasaki and Y. Matsumi, *Bull. Chem. Soc. Jpn.*, 1998, **71**, 2539.
26 Our design is based on the original design by Prof. D. Gerlich (http://www.tu-chemnitz.de/physik/ION/Technology/Piezo_Valve/index.html).
27 A. T. J. B. Eppink and D. H. Parker, *Rev. Sci. Instrum.*, 1997, **68**, 3477.
28 G. A. Garcia, L. Nahon and I. Powis, *Rev. Sci. Instrum.*, 2004, **75**, 4989.
29 V. Loriot, L. Bañares, R. de Nalda, 2011, unpublished.
30 R. O. Roos, *The Complete Active Space Self-Consistent Field Method and its Applications in Electronic Structure Calculations*, in *Advances in Chemical Physics: Ab initio Methods in Quantum Chemistry Part 2*, ed. K. P. Lawley, John Wiley & Sons, Inc., Hoboken, NJ, USA, 2007, vol. 69.
31 J. Finley, P. Malmqvist, B. O. Roos and L. Serrano-Andrés, *Chem. Phys. Lett.*, 1998, **288**, 299.
32 D. Ajitha, M. Wierzbowska, R. Lindh and P. A. Malmqvist, *J. Chem. Phys.*, 2004, **121**, 5761.
33 P. O. Widmark, P. Malmqvist and B. O. Roos, *Theor. Chim. Acta*, 1990, **77**, 291.
34 P. O. Widmark, B. J. Persson and B. O. Roos, *Theor. Chim. Acta*, 1991, **79**, 419.
35 B. O. Roos, R. Lindh, P. Malmqvist, V. Veryazov and P. Widmark, *J. Phys. Chem. A*, 2004, **108**, 2851.
36 B. O. Roos and K. Andersson, *Chem. Phys. Lett.*, 1995, **245**, 215.
37 C. M. Marian and U. Wahlgren, *Chem. Phys. Lett.*, 1996, **251**, 357.
38 G. Karlström, *et al.*, *Comput. Mater. Sci.*, 2003, **28**, 222.
39 G. A. Bogdanchikov, A. V. Baklanov and D. H. Parker, *Chem. Phys. Lett.*, 2003, **376**, 395.
40 A. Weigand, X. Cao, J. Yang and M. Dolg, *Theor. Chem. Acc.*, 2009, **126**, 117.
41 J. Chen, L. S. Pei, J. N. Shu, C. X. Chen, X. X. Ma, L. S. Shen and Y. W. Zhang, *Chem. Phys. Lett.*, 2001, **345**, 57.
42 L. Poth, Q. Zhong, J. V. Ford and A. W. Castleman Jr, *J. Chem. Phys.*, 1998, **109**, 4791.
43 R. de Nalda, J. G. Izquierdo, J. Durá and L. Bañares, *J. Chem. Phys.*, 2007, **126**, 021101.
44 R. N. Zare, *Angular Momentum Understanding Spatial Aspects in Chemistry and Physics*, Wiley, New York, 1998.
45 J. A. Syage, *Chem. Phys. Lett.*, 1995, **245**, 605.
46 J. A. Syage, *Chem. Phys.*, 1996, **207**, 411.
47 G. C. G. Waschewsky, R. Horansky and V. Vaida, *J. Phys. Chem.*, 1996, **100**, 11559.
48 D. Ajitha, D. G. Fedorov, J. P. Finley and K. Hirao, *J. Chem. Phys.*, 2002, **117**, 7068.

